








Exploring Neutral Hydrogen in Radio MOlecular Hydrogen Emission Galaxies (MOHEGs) and Prospects with the SKA

Sai Wagh¹ , Mamta Pandey-Pommier^{2,3} , Nirupam Roy¹ , Md Rashid¹ , Alexandre Marcowith² ,
Chinnathambi Muthumariappan⁴, Ramya Sethuram⁴, Subhashis Roy⁵, and Bruno Guiderdoni⁶

¹ Indian Institute of Science, CV Raman Road, Bangalore-560012, India; saiwagh@iisc.ac.in

² CNRS/Laboratoire Univers et Particules de Montpellier, Université de Montpellier LUPM CC 072—Place Eugène Bataillon 34095 Montpellier Cedex 5, France

³ Catholic University of Lyon, 10, place des Archives 69288 Lyon Cedex 02, France

⁴ Indian Institute of Astrophysics, II Block, Koramangala, Bangalore 560034, India

⁵ National Centre for Radio Astrophysics—Tata Institute of Fundamental Research, Ganeshkhind, Pune 411007, Maharashtra, India

⁶ Université de Lyon, Univ Lyon1, Ens de Lyon, CNRS, Centre de Recherche Astrophysique de Lyon UMR5574, F-69230, Saint-Genis Laval, France

Received 2023 November 24; revised 2024 January 9; accepted 2024 January 14; published 2024 March 4

Abstract

Empirical studies of cold gas content are essential for comprehending the star formation activities and evolution in galaxies. However, it is not straightforward to understand these processes because they depend on various physical properties of the interstellar medium. Massive Faranoff–Riley I/II type radio galaxies rich in molecular hydrogen with lower star formation activities are known as radio molecular hydrogen emission galaxies (MOHEGs). We present a study of neutral hydrogen-gas-associated radio MOHEGs at redshifts <0.2 probed via the HI 21 cm absorption line. Neutral hydrogen is detected in 70% of these galaxies, which are located at a distance of 8–120 kpc from the neighboring galaxies. These galaxies show a scarcity of HI gas as compared to merging galaxies at similar redshifts. We found no strong correlation between $N(\text{HI})$, N_{H} , and the galaxy properties, regardless of whether the HI is assumed to be cold or warm, indicating that the atomic gas probably plays no important role in star formation. The relation between the total hydrogen gas surface density and the star formation surface density deviates from the standard Kennicutt–Schmidt law. Our study highlights the importance of HI studies and offers insights into the role of atomic and molecular hydrogen gas in explaining the properties of these galaxies. In the upcoming HI 21 cm absorption surveys with next-generation radio telescopes such as the Square Kilometre Array and pathfinder instruments, it may be possible to provide better constraints for these correlations.

Unified Astronomy Thesaurus concepts: [Star formation \(1569\)](#); [Faranoff-Riley radio galaxies \(526\)](#)

1. Introduction

Gas interactions between galaxies and the intracluster medium (ICM) play a crucial role in star formation activities and their evolution. Galaxies experience several interactions that influence their evolution over cosmic time, such as gravitational interaction and merger events among the nearest neighbors, tidal forces between neighboring galaxies, ram pressure stripping, and strangulation in dense environments (Toomre 1974; Alladin 1975; Kawata & Mulchaey 2008; Weżgowiec et al. 2012; Peng et al. 2015; Boselli et al. 2022). These interactions can either trigger bursts of star formation and fuel the central supermassive black holes (SMBHs), stripping away their gas and leading to a gradual loss of fuel and quenching of star formation. It eventually results in morphological changes from the stage of gas-rich star-forming (SF) galaxies with extended disks to quiescent ellipticals (Lada 2005; Vollmer 2013; Guglielmo et al. 2015; Pearson et al. 2019). The lack of cold gas and quenching of star formation is often associated with the heating of the gaseous ICM to millions of Kelvin through feedback processes. In bright central galaxies (BCGs) in galaxy clusters, a part of the molecular gas undergoes star formation, but the rest of the gas is expected to accrete onto the central SMBH, which ignites the active galactic nucleus (AGN) radio jet feedback activities.

Feedback via AGN hosting SBMH at the centers of galaxies that accrete gas and release tremendous amounts of kinetic energy via radio-jets dissipates through shocks, resulting in a turbulent heating of the molecular gas and reducing the star formation efficiency in the surrounding ICM (Antonuccio-Delogu & Silk 2008; Cielo et al. 2018). The mechanism of sweeping out gas from their host galaxies, i.e., negative feedback, prevents the cooling and condensation of gas onto galaxies, thereby regulating the amount of cold molecular gas that is available for star formation and the properties of the intergalactic medium (Fabian 1994; Fujita et al. 2022). On the other hand, jet activities can also compress gas within the interstellar medium (ISM) and trigger star formation in dense cluster regions. This gives rise to a positive feedback mechanism, thereby enhancing star formation (Silk 2013; Maiolino 2017). The other mechanism of heating the ISM is feedback via explosive supernova events, which are responsible for driving powerful winds and shock waves to expel cold gas from galaxies. However, supernova feedback is more relevant in lower-mass galaxies and can significantly impact their evolution (Li et al. 2015; Martizzi et al. 2015). In addition to this, high-velocity gas outflows in mergers have been reported as a result of quasi-stellar object (QSO) mode feedback, and it can contribute strongly to powering the AGN winds in mergers (Narayanan et al. 2008; Rupke & Veilleux 2011; Veilleux et al. 2017). The connection between these feedback processes responsible for heating the ICM and the availability of cold molecular gas reservoirs is crucial for developing a comprehensive picture of the influence of



Original content from this work may be used under the terms of the [Creative Commons Attribution 4.0 licence](#). Any further distribution of this work must maintain attribution to the author(s) and the title of the work, journal citation and DOI.

different environments on star formation and galaxy evolution (Man & Sirio 2018).

One of the substantial factors that governs star formation in galaxies is the availability of cold (atomic + molecular) gas. The molecular gas (H_2) distribution within the ISM directly impacts star formation, which further depends upon the reserve of atomic hydrogen (H I) that is available. In the ISM, H I leads to the formation of H_2 through an exothermic process. Theoretical models such as the Langmuir–Hinshelwood (LH) and Eley–Rideal (ER) models have been proposed to understand the process of H I to H_2 transformation. Interstellar dust grains and polycyclic aromatic hydrocarbons (PAHs) act as catalysts in these processes; they act as surfaces over which hydrogen atoms can be readily absorbed and diffused, enabling the three-body reaction, which is much more efficient than the gas-phase reaction (Vidali 2013; Foley et al. 2018; Thi et al. 2020; Park et al. 2023). In late-type galaxies, the Kennicutt–Schmidt (KS) law suggests a direct proportionality between the surface density of the star formation rate and the positive power of cold gas surface densities within their ISM (Schmidt 1959, 1963; Kennicutt 1998a). Moreover, the atomic phase of hydrogen in galaxies acts as a crucial intermediary constituent in the baryon cycle, directly influencing structural evolution and star formation activities in these systems. Gas-rich galaxy disks hold extended atomic gas in their disk regions, which is susceptible to distortions during tidal interactions. The effects of these activities can be studied through observations of the H I 21 cm transition (Yun et al. 1994; Noordermeer et al. 2005; Chung et al. 2009; Brown et al. 2017; Dutta et al. 2022). Additionally, observations of atomic gas outflows in radio galaxies (RG) suggest that AGN radio jet feedback has a galaxy-scale impact on the host ISM (Morganti et al. 2003, 2005; Guillard et al. 2012; Schulz et al. 2021). This implies that atomic gas is also influenced by chemical, radiative, and mechanical feedback associated with star formation activities (Cox & Smith 1974; Wolfire et al. 1995; Naab & Ostriker 2017).

The atomic ISM traced by the H I 21 cm in galaxies exists in two different phases: the cold neutral medium (CNM), having densities $\geq 10 \text{ cm}^{-3}$ and spin temperatures $\leq 200 \text{ K}$, and the warm neutral medium (WNM), with densities around $\approx 0.1\text{--}1 \text{ cm}^{-3}$ and spin temperatures $\geq 5000 \text{ K}$ (Clark 1965; Wolfire et al. 2003; Saury et al. 2014). The gas densities decide the physical conditions of the atomic phases in the ISM. Below $N(\text{H I}) \leq 10^{17} \text{ cm}^{-2}$ column densities, the gas is optically thin and is ionized by UV photons, giving rise to Ly α emission lines; the spectra are known as the Ly α forest (Rauch 1998). At the range of $10^{17} \text{ cm}^{-2} \leq N(\text{H I}) \leq 10^{20} \text{ cm}^{-2}$, gas becomes optically thick, and the core of Ly α is saturated. Systems like this are called Lyman-limit systems (Bergeron & Boissé 1991). At the same time, there are damped Ly α absorbers (DLAs) having $N(\text{H I}) \geq 10^{20} \text{ cm}^{-2}$, where the Ly α line becomes optically thick in its naturally broadened wings (Wolfe et al. 2005). A threshold neutral hydrogen column density of $N(\text{H I}) \sim 5 \times 10^{20} \text{ cm}^{-2}$ is required to begin with the formation of H_2 , which helps to shield the gas against radiation from UV photons (Stecher & Williams 1967; Hollenbach et al. 1971; Federman et al. 1979; Kanekar et al. 2011). Unlike the H I emission lines, where the flux attenuates with distance, H I absorption features are independent of the distance of the source; rather, they primarily depend on the strength of the background radio continuum, the covering fraction (f_c) of the source, and the spin temperature T_s (K)

(Dutta et al. 2022). Hence, the H I 21 cm absorption line studies can complement the emission line surveys to trace the evolution of the atomic gas component in and around galaxies. The H I 21 cm optical depth-integrated over velocity ($\tau(v)dv$) is proportional to the column density of neutral hydrogen, $N(\text{H I}) \text{ cm}^{-2}$, given by

$$N_{\text{HI}} = 1.82 \times 10^{18} \cdot \frac{T_s}{f_c} \int \tau(v) dv (\text{cm}^{-2}), \quad (1)$$

where T_s (K) is the spin temperature of the gas, and f_c is the fraction of the background radio source covered by the absorbing gas (Rohlfs & Wilson 2000), and dv is in km s^{-1} .

Ogle et al. (2007) found enhanced molecular emission from purely rotational line emission $L(\text{H}_2) = (8.0 \pm 0.4) \times 10^{41} \text{ erg s}^{-1}$ from a radio galaxy system (3C 326N). Many more galaxies observed with Spitzer showed this enhanced H_2 emission, leading to their classification as molecular hydrogen emission galaxies (MOHEGs). Cluver et al. (2013) investigated 23 highly compact galaxies (HCGs) with Spitzer, 14 of which are MOHEGs. Studies from the Spitzer Infrared (IR) telescope have revealed H_2 purely rotational emission lines detected from their warm (100–1500 K) molecular gas up to a redshift of $z < 0.22$ with an $L(\text{H}_2)/L(\text{PAH})$ ratio (0.03–4 or greater). Up to a factor of ~ 300 , this ratio is greater than that of normal SF galaxies. These galaxies with FR-I and FR-II type radio morphologies are called radio MOHEGs (Ogle et al. 2010). The measured purely rotational and rovibrational H_2 transitions measured in these galaxies indicated H_2 luminosities in the range of $10^{40}\text{--}10^{42} \text{ erg s}^{-1}$, which act as the primary coolant for the warm molecular phase of the ISM, which is characterized by short cooling timescale ($\sim 10^4$ years; Le Bourlot et al. 1999; Maret et al. 2009). Despite possessing a substantial amount of molecular hydrogen gas ($\sim 10^{10} M_\odot$), these galaxies exhibit inefficient star formation. This suggests that the excess molecular gas is kinematically unsettled and turbulent, hindering its cooling and star formation processes.

There is uncertainty regarding the origin of the large quantities of molecular gas in radio MOHEGs. Additionally, these galaxies are found either in dense galaxy cluster environments or in close interacting pairs or groups, which are expected to be stripped of their H I gas content. However, the observed high molecular mass in these galaxies indicates enhanced cooling flows that drive gas into their central regions (Ogle et al. 2007). Thus, for a complete picture of the neutral and molecular hydrogen gas content in these galaxies as well as the impact of possible interactions on star formation, we studied a sample of 10 radio MOHEGs with H I absorption data available in the literature. This paper presents the study of the distribution of neutral hydrogen gas in a sample of 10 radio MOHEGs, exploring the global H I absorption and total hydrogen gas properties. We also explore the correlation between hydrogen gas and various galaxy properties, and we present their relations with star formation. The rest of this paper is organized as follows: Section 2 describes the radio galaxy sample and provides details of the H I absorption data. Section 3 presents the results of the study of neutral hydrogen gas distribution in our radio MOHEG sample, highlighting its association with galaxy properties, and it investigates whether radio jet-induced feedback might heat the molecular gas. In Section 4 we discuss the potential role of upcoming telescopes such as the Square Kilometer Array (SKA) and its precursors in addressing the H I to H_2 phase related to MOHEG-type

Table 1
Observation Details of the Radio MOHEG Catalog

Source (1)	Type (2)	z (3)	Observations (4)	References (5)
Cen A	I, TJ	0.00183	HIPASS	Allison et al. (2014)
3C 31	I, TJ	0.01701	VLA-C	Moss et al. (2017)
3C 84	I, FD	0.01756	JLVA-A	Morganti et al. (2023)
3C 218	I, TJ	0.05488	VLA-A	Dwarakanath et al. (1995)
3C 270	I, TJ	0.00747	VLA-C	Jaffe & McNamara (1994)
3C 293	I, CSC	0.04503	WSRT	Geréb et al. (2015)
3C 317	I, FD	0.03446	VLA-A	van Gorkom et al. (1989)
3C 338	Ip, FD	0.03035	GMRT	Chandola et al. (2013)
3C 405	II	0.05608	VLBA + phased VLA	Struve & Conway (2010)
3C 433	II, X	0.10160	Arecibo	Curran et al. (2016)

Note. Column (1): object name (NED). Column (2): radio morphologies according to the Fanaroff & Riley (1974) classification; where I is FR-I type, and II is FR-II type, p: peculiar, TJ: twin jet, FD: fat double, CSC: compact symmetric core, DD: double-double, X: “X” shaped. Column (3): redshift (NED). Column (4): HI observations. Column (5): references for HI observations.

galaxies through deeper HI observations. Finally, Section 5 summarizes our results and conclusions.

Throughout this work, we consider a flat Λ -CDM cosmology with the Hubble constant $H_0 = 70 \text{ km s}^{-1} \text{ Mpc}^{-1}$ and the matter density parameter $\Omega_M = 0.30$.

2. Sample and Data Selection

This study is based on a sample of radio MOHEGs with excess H_2 gas detected in Spitzer IR Spectrograph observations (Ogle et al. 2010). The radio counterpart of these galaxies shows galaxies with FR-I and FR-II type morphologies lying at $z < 0.2$ (from the 3C RR and 3C R catalogs). Out of 17 H_2 detected MOHEG sources from Ogle et al. (2010), we recovered HI absorption data for 10 sources from the existing literature and from the GMRT, VLA, WSRT, and Arecibo archives as listed in Table 1. The remaining seven sources, 3C 310, 3C 315, 3C 272.1, 3C 386, 3C 436, 3C 424, and 3C 326N, have not been observed earlier in the L band for HI studies, and future observations for these sources will be proposed with existing and upcoming radio telescopes (e.g., SKA, VLA, MeerKat, and uGMRT) to understand the atomic gas kinematics of radio MOHEGs. In this paper, we study the HI gas properties of 10 H_2 detected radio MOHEGs. The hydrogen gas (both HI and H_2) properties for our sample are listed in Table 2. The HI column densities we calculated are the average of column densities along adjacent lines of sight against multiple components of the continuum, but for Arecibo observations, the sources are not resolved due to the coarse resolution of $3/5$ offered by this instrument (Knapp et al. 1978; Colgan et al. 1990). The total hydrogen column densities and molecular hydrogen fraction for our sample were computed using the following equations (Winkel et al. 2017):

$$N_{\text{H}} = N_{\text{HI}} + 2N_{\text{H}_2} \quad (2)$$

and

$$f_{\text{H}_2} = \frac{2N_{\text{H}_2}}{2N_{\text{H}_2} + N_{\text{HI}}} \quad (3)$$

The molecular hydrogen fraction f_{H_2} was calculated for these galaxies across a spectrum of spin temperatures ranging from 100 to 1500 K. We aim to understand the change in molecular fraction with the varying spin temperature of the HI gas. To understand the interaction of these galaxies with the surrounding environments in our sample, one way is to consider the distances from the cluster centers or the distances to the nearest neighbors. All of our sources have neighbors at a distances of a few kiloparsec. Moreover, 7 of the 10 sources reside inside clusters, and in these cases, the distance from the cluster center may be a better proxy for studying the interaction effects. Except for two sources, however, all of the sources residing in the cluster have neighboring galaxies nearer than the cluster center. Therefore, we choose the nearest-neighbor distances to study the interaction effects homogeneously. We searched for the nearest-neighbor galaxies at a similar redshift as radio MOHEGs in the NASA NED archive database. The maximum velocity difference between our sources and the nearest neighbors is 1388 km s^{-1} . We converted the projected angular separations into projected linear separations (in kiloparsec) using the conversion scales obtained from Ned’s Cosmological Calculator (Wright 2006), as listed in Table 2. The radio luminosities at 178 MHz are an excellent proxy for AGN radio jet powers because in this band, the total flux measured is synchrotron in origin, dominated by emission from the jet region. Finally, the star formation rates (SFRs) were computed from the $7.7 \mu\text{m}$ PAH, the $11.3 \mu\text{m}$ PAH emission lines observed in the IR Spitzer spectroscopic data, or from the $70 \mu\text{m}$ Herschel Photoconductor Array Camera and Spectrometer (PACS)/Spitzer Multiband Imaging Photometer (MIPS) photometric data. The median properties for our sample are $z = 0.0324$, a projected separation of $\rho = 13.78 \text{ kpc}$, a radio luminosity of $\nu L_{178} = 1.55 \times 10^{41} \text{ erg s}^{-1}$, and an SFR = $0.52 M_{\odot} \text{ yr}^{-1}$. We also investigated the association between the gas column densities and global properties of the radio MOHEGs sample, as listed in Table 3.

3. Results and Discussion

The HI 21 cm absorption lines are powerful tracers of cold gas in the central regions (at parsec scales), close to the central black hole of galaxies and up to tens of kiloparsec. They trace interaction and mergers into galaxy groups as well as the intervening neutral gas clouds in foreground galaxies, tails, and filaments (Morganti & Osterloo 2018; Dutta et al. 2022). HI absorption in radio sources is mostly detected against the central regions, allowing us to probe the gas properties in the inner regions of the sources and the AGN structures. Below, we discuss the results of our investigation of the HI absorption properties of MOHEG galaxies, the influence of the environment on their merger activities, and the impact of radio-mode feedback on the gas properties.

3.1. Distribution and Kinematics of HI Gas

The average column density for HI disks in spiral galaxies is approximately $6 \times 10^{20} \text{ cm}^{-2}$ (Wang et al. 2016). On the other hand, early-type galaxies (ETGs) tend to have HI column densities of 10^{20} cm^{-2} at most (Serra et al. 2012). In a sample of nearby radio galaxies, these values range from

Table 2
Hydrogen Gas in Radio MOHEGs Sample

Source	$N(\text{H I})$	N_{H_2}	N_{H}	f_{H_2}				F_{178}	$\log \nu L_{178}$	Nearest Neighbor
	(10^{20}) cm^{-2}	(10^{20}) cm^{-2}	(10^{22}) cm^{-2}	I	II	III	IV	Jy	erg s^{-1}	Distances (ρ) kpc
(1)	(2)	(3)	(4)	(5)	(6)	(7)	(8)	(9)	(10)	(11)
Cen A	5.70	1150	23.10	0.99	0.99	0.96	0.83	1005	40.12	8.25
3C 31	<0.60	88.3	<1.77	<0.99	<0.99	<0.99	<0.97	18.3	40.33	5.81
3C 84	2.40	<302	<6.06	<0.99	<0.99	<0.98	<0.93	66.8	40.92	29.51
3C 218	7.00	82.0	1.71	0.96	0.96	0.89	0.66	225.7	42.46	9.86
3C 270	7.20	<50.3	<1.08	<0.93	<0.93	<0.74	<0.49	53.4	40.07	16.84
3C 293	14.50	215	4.41	0.97	0.97	0.86	0.72	13.8	41.07	119.85
3C 317	<1.62	<20.3	<0.42	<0.96	<0.95	<0.85	<0.63	53.4	41.42	5.77
3C 338	<5.59	<30.1	<0.65	<0.92	<0.92	<0.67	<0.42	51.1	41.28	18.97
3C 405	23.1	<200	<4.23	<0.95	<0.92	<0.75	<0.54	9483	44.10	10.72
3C 433	2.30	310	6.22	0.99	0.99	0.99	0.98	61.3	42.46	29.62

Note. Column (1): object name (NED). Column (2): average $N(\text{H I})$ of the detections and 3σ upper limits on nondetections for T_s of 100 K. Column (3): total N_{H_2} of the detections and 3σ upper limits on nondetections (Ogle et al. 2010). Column (4): total hydrogen column densities. Column (5): molecular fraction computed for $N(\text{H I})$ assuming a spin temperature of 100 K. Column (6): 100–160 K. Column (7): 250–680 K. Column (8): 1100–1500 K. Column (9): 178 MHz flux densities (Baars et al. 1977). Column (10): radio luminosity at 178 MHz (Ogle et al. 2010). Column (11): nearest-neighbor angular separation taken from NASA NED. We used the scale (NED WRIGHT Cosmological Calculator, Wright 2006) to convert the distances into kiloparsec.

Table 3
Correlation Analysis between the Hydrogen Gas and Various Galaxy Properties of the Radio MOHEG Sample

Variables	$N(\text{H I})$					N_{H}					f_{H_2}		SFR
	τ_k	p_k	m_t	τ_k	p_k	m_t	τ_k	p_k	m_t	τ_k	p_k	m_t	
(1)	(2)	(3)	(4)	(5)	(6)	(7)	(8)	(9)	(10)	(11)	(12)	(13)	
ρ	0.20	0.47	0.3274	0.15	0.56	0.7685	0.04	0.92	0.0036	0.46	0.06	0.2786	
νL_{178}	0.08	0.78	0.0736	0.00	1.00	-0.0072	-0.11	0.69	-0.0041	0.17	0.51	0.2255	
z	0.13	0.64	8.1013	0.11	0.69	0.4279	0.00	1.00	0.0174	0.28	0.26	12.2154	

Note. Column (1): correlation between the properties (ρ , L_{178} and z) of the radio MOHEGs sample and $N(\text{H I})$, N_{H} , f_{H_2} , and SFR tested using nonparametric correlation tests. Columns (2), (5), (8), and (11): Kendall's Tau rank correlation coefficient. Columns (3), (6), (9), and (12): the p -values. Columns (4), (7), (10), and (13): Akritas–Theil–Sen slope. These tests were made with the R software using the cenken function from the NADA package, especially for censored data points in the survival analysis.

10^{20} to 10^{21} cm^{-2} , with an assumed spin temperature of $T_s = 100 \text{ K}$ (Emonts et al. 2010). Radio MOHEGs show a wide range of HI column densities spanning from $\approx 6 \times 10^{19} \text{ cm}^{-2}$ to $2.31 \times 10^{21} \text{ cm}^{-2}$. Hence, radio MOHEGs exhibit column densities that contrast with those of spirals and ETGs. Nevertheless, the recorded HI column densities in radio MOHEGs remain lower than those found in Seyfert galaxies, where the column densities can reach up to 10^{22} cm^{-2} (Morganti & Osterloo 2018). In 7 of the 10 galaxies in our sample, neutral hydrogen is detected, with HI column densities reaching as low as 10^{20} cm^{-2} , which is the highest temperature of H_2 estimated for this source (Ogle et al. 2010). Figure 1 shows the column density of HI versus the nearest-neighbor distance (left) and redshift (right) for radio MOHEGs and a sample of mergers (Dutta et al. 2019) for comparison.

From the left panel of Figure 1, we see that radio MOHEGs have nearest-neighbor distances of 5–120 kpc, which fall in the same range as the projected separation of pre-mergers and ongoing mergers. Hence, we suggest that radio MOHEGs are engaged in ongoing mergers and pre-merger stages. Moreover, the median HI column densities are $5.65 \times 10^{20} \text{ cm}^{-2}$, but the upper detection limits suggest that the HI column densities can be much lower in radio MOHEGs. The median $N(\text{H I})$ value for the merger sample lies at $\sim 5 \times 10^{21} \text{ cm}^{-2}$, which is

approximately nine times higher than the median $N(\text{H I})$ value observed in radio MOHEGs. From the above results, we infer that radio MOHEGs exhibit a deficiency in atomic hydrogen compared to merging galaxies at similar redshifts. The right panel of Figure 1 explains that there is no preferential distribution of $N(\text{H I})$ with redshift between radio MOHEGs and merger samples. However, the redshift range is too small to rule out any such trend conclusively. In addition, previous studies have shown that galaxies residing in galaxy clusters tend to have a lower neutral hydrogen content than similar types of galaxies lying in isolated fields; mechanisms such as ram pressure stripping and tidal interactions could explain this HI deficiency (Denes et al. 2016).

3.2. Hydrogen Gas and Galaxy Properties

We carried out nonparametric correlation tests to study the association between hydrogen gas properties and galaxy properties such as radio jet luminosities, redshift, and the effects of the host environment. The results of the Kendall's Tau correlation coefficient (τ_k) and the probability values (p -values, p_k) verify whether the correlation is statistically significant. The association and probability values between the physical parameters are presented in Table 3, along with Akritas–Theil–Sen slopes (m_t), with the aim to find the best fit, giving an unbiased estimate of the correlation trend magnitude

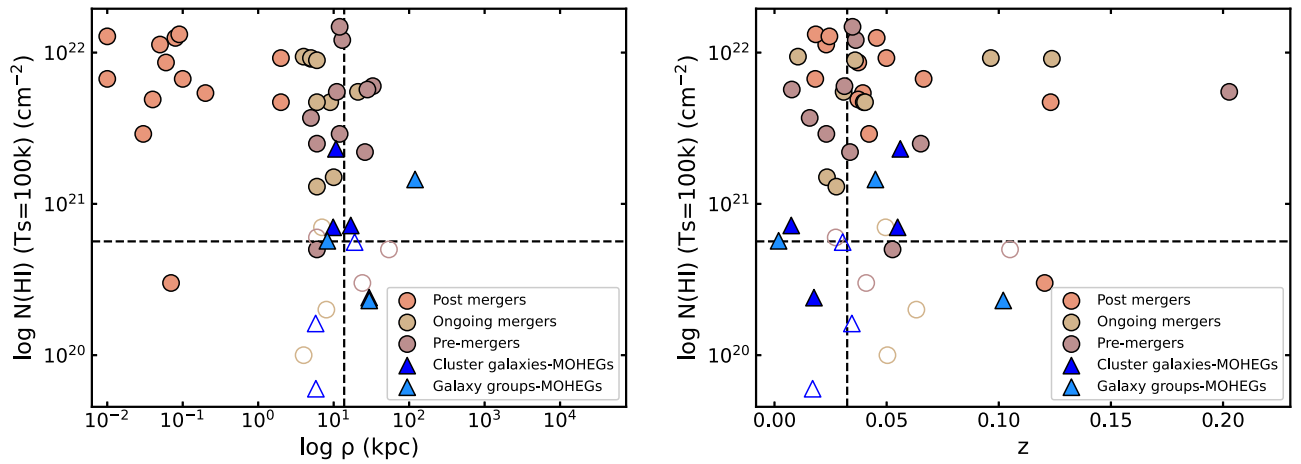


Figure 1. Comparison of neutral hydrogen column densities with the nearest-neighbor distance (shown in the left panel) and redshift (shown in the right panel) between the radio MOHEG sample (represented as blue triangles) and a set of merger samples (represented as circles) sourced from Dutta et al. (2019). The colored markers represent instances of H I detections in the data set, and empty markers indicate H I nondetections, considering 3σ sensitivity levels. The dashed lines correspond to the median values extracted from the radio MOHEG sample, with medians of $N(\text{H I}) \leq 5.65 \times 10^{20} \text{ cm}^{-2}$, $z = 0.03245$, and $\rho = 13.78 \text{ kpc}$.

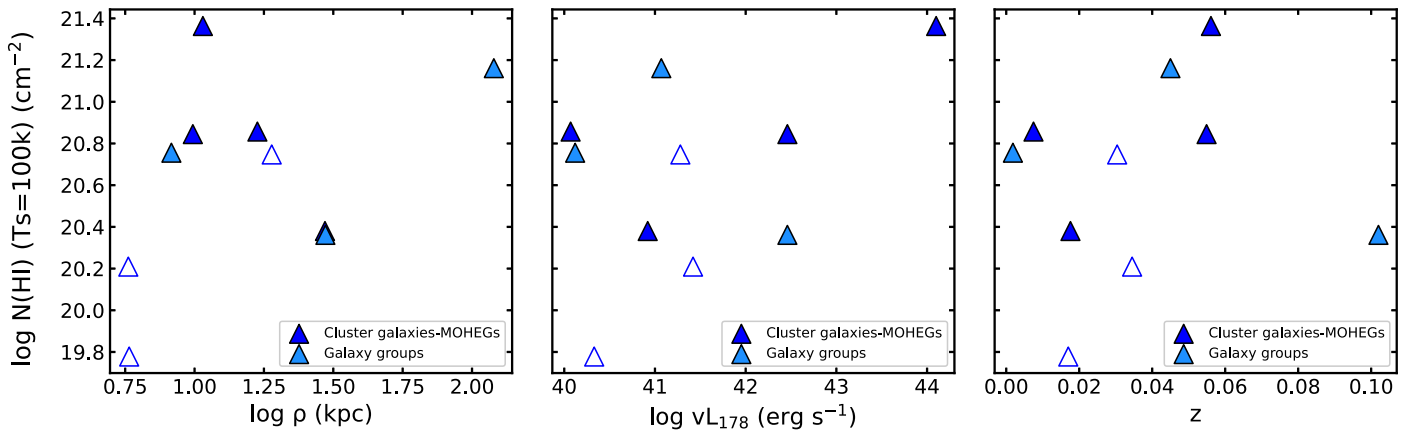


Figure 2. The inferred $N(\text{H I})$ values for radio MOHEGs are presented with the projected separation, 178 MHz radio luminosity, and redshift, sequentially from left to right. Filled symbols represent cases of detection, and empty symbols denote the 3σ upper limits. Based on the Kendall's Tau nonparametric test, $N(\text{H I})$ exhibits no correlation with these parameters, as detailed in Table 3.

with a better asymptotic efficiency than the least-squares estimation. We do not find any significant correlation between the global H I or H I + H₂ gas profiles with those of the galaxy properties. We note that the results presented in Table 3 used $N(\text{H I})$ estimated assuming an average $T_s = 100 \text{ K}$. However, qualitatively, the lack of correlations is found to be independent of this assumption. When we consider the extreme scenario that the absorptions instead arise from H I with T_s in the range of 1100–1500 K (i.e., the same as the highest temperature of H₂ for the corresponding source from Ogle et al. 2010), there is no qualitative change in our results. This suggests that comprehending the triggering or quenching of nuclear star formation and its dependence on hydrogen gas in the central regions of these galaxies based on H I absorption properties poses a challenge. The maximum correlation measured between all the derived quantities and the galaxy properties is between the SFRs, and the nearest-neighbor distances is 0.46, which implies a weak correlation. In this case, we have obtained a p -value of 0.06, which is very close to 0.05, and we suggest that these two quantities are possibly weakly correlated. This would imply a weak dependence of the star formation activities on the surrounding environments.

As presented in Table 3, we observe no correlation between the interaction distance on the H I column densities in our sample despite galaxy collisions or tidal interactions from neighboring galaxies that should make the ISM gas rich. As seen in the merger sample of Dutta et al. (2019), $N(\text{H I})$ has a weak dependence on the projected separations, although as seen in Figure 2 (Panel 1), we see no such association here. Further, we expect that the AGN radio jet feedback should expel the gas from the central regions of galaxies, making them deficient in neutral gas. We find no strong association of $N(\text{H I})$ with the radio jet luminosity from a high p -value of ~ 0.8 in the radio MOHEG sample, as seen in Figure 2 (Panel 2). However, Nesvadba et al. (2010) and Guillard et al. (2012) inferred that AGN feedback drives H I outflows in samples of molecular gas-rich radio galaxies. Ionized and atomic gas is well coupled dynamically and is outflowing at comparable velocities in these systems. 3C 293, one of the radio MOHEGs, shows broad blueshifted H I absorption, indicating a fast outflow of neutral gas that could originate near AGNs (Morganti et al. 2003). Moreover, ionized gas outflows from this system are reported (Mahony et al. 2016). However, we do not know how the molecular gas is affected (Guillard et al. 2012). Until now, most observations of neutral hydrogen in galaxies have been

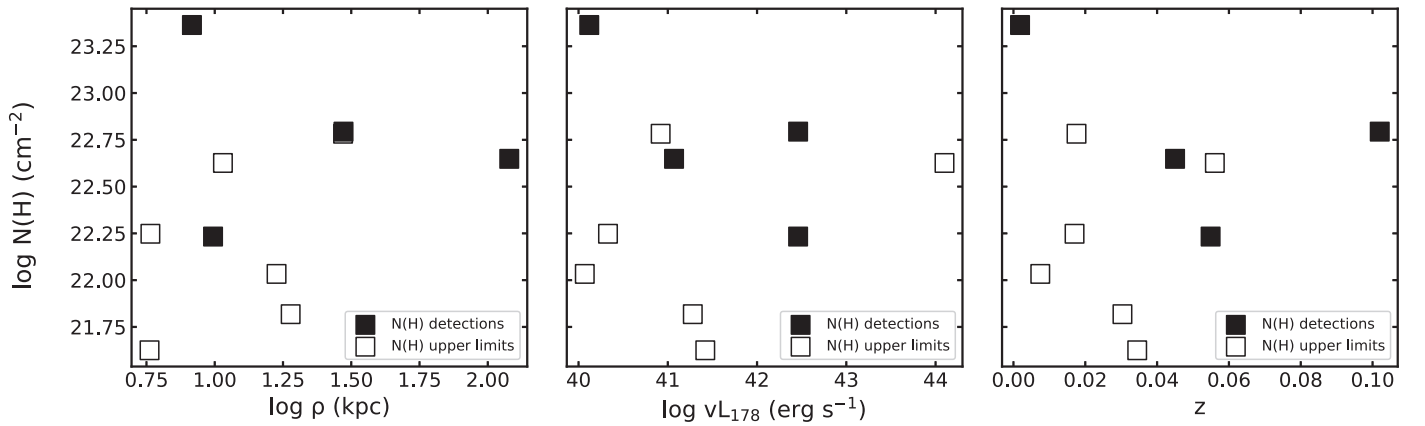


Figure 3. The inferred N_{H} values for radio MOHEGs are presented vs. projected separation, 178 MHz radio luminosity, and redshift, sequentially from left to right. The filled symbols represent cases of detection, and empty symbols denote the 3σ upper limits. Based on the Kendall's Tau nonparametric test, N_{H} exhibits no correlation with these parameters, as detailed in Table 3.

conducted with limited sensitivity and narrow frequency ranges, constraining the detection of high-velocity HI outflows. Detailed kinematic investigations of HI can be conducted with high resolution, high sensitivities, and wider bandwidths, enabling the identification of broader and shallower absorption features. These AGN-induced outflows draw out the neutral gas from central regions in these systems, and the part of the bulk kinetic energy of the outflowing neutral gas can be transferred into molecular gas heating through shocks in the ISM. No HI or H_2 outflows have been reported for our sample so far (except for 3C 293); it will be intriguing to see whether AGN-induced neutral gas outflows are also responsible for heating the molecular gas in radio MOHEGs. For two radio MOHEGs, 3C 293 and 3C 338, restarted radio jet activities have been reported (Gentile et al. 2007; Mahony et al. 2013), but none of the other sources have broadband measurements to study the interplay between jets and the environment. We do not observe a correlation of the total hydrogen gas column densities (N_{H}) with the other properties of radio MOHEGs either (see Figure 3). However, understanding the total hydrogen content in these sources can provide valuable information about the ongoing and future star formation capacities. The distinction between the scatter in the data points and the fit could arise due to the limited scope of our sample, where the extent of the observations significantly affects the correlation analysis. Nevertheless, studying the effects of negative and positive AGN feedback in radio MOHEGs, which introduce turbulence within the ISM and potentially govern the HI content, is essential.

3.3. Molecular Fraction and Star Formation Rates

To gain insights into the combined presence of HI and H_2 gas within the ISM, we examined the molecular hydrogen fraction (f_{H_2}) within the radio MOHEG sample. This fraction reveals the proportions of H_2 and other molecular gases in the ISM. By investigating the dependence of radio MOHEG properties on this molecular fraction, we aim to enhance our understanding of the efficiency of converting HI into H_2 and its effects on star formation processes. In the context of radio MOHEGs, when $N(\text{HI})$ is computed using T_s of 100 K, the average molecular fraction is ≤ 0.96 . This fractional value implies that the hydrogen gas in radio MOHEGs is dominated by molecular gas. As listed in Table 2, the molecular fraction

diminishes when the neutral gas temperature varies with the temperature range where warm molecular gas is found. Furthermore, the correlation between the molecular hydrogen fraction and SFRs within radio MOHEGs implies no association, characterized by a correlation coefficient of 0.22. A robust power-law relation has been identified between the local molecular gas fraction and the pressure of the ISM among nearby galaxies, rich in both HI and H_2 gas, as well as dwarf galaxies (Blitz & Rosolowsky 2004, 2006). Leroy et al. (2008) focused on 23 HI galaxies from THINGS, confirming a power-law connection between f_{H_2} and the interstellar gas pressure, characterized by a power-law index of 0.8. However, our results signify no molecular fraction dependence on the galaxy properties of radio MOHEGs.

In Figure 4 we present the correlation between the SFRs and the physical properties of the radio MOHEG sample. The SFRs exhibit a weak correlation with the nearest-neighbor distances ($\tau_k = 0.46$), suggesting that close-range galaxy interactions might lead to a decrease in star formation activities within radio MOHEGs due to the potential heating of molecular gas. This could be influenced by the negative feedback resulting from interactions and collisions with neighboring galaxies (Kennicutt 1998b; Pan et al. 2018). In panel 2 of Figure 4, despite a relatively low correlation value ($\tau_k \sim 0.17$), the higher value of SFRs tends to align with the higher values of radio luminosities. We note that galaxies with a higher mass might exhibit elevated radio luminosities and increased SFRs, but this does not necessarily mean that the luminosities directly influence the star formation activities.

3.4. Star Formation Relations

To comprehend the star formation activities in radio MOHEGs, we investigated the relations between the surface density of star formation (Σ_{SFR}) and hydrogen gas surface densities. The empirical relation that characterizes the correlation between the star formation density and the hydrogen gas surface density in galaxies is known as the KS law of star formation (Schmidt 1959), given by Equation (4),

$$\Sigma_{\text{SFR}} = A \Sigma_{\text{gas}}^N, \quad (4)$$

where (Σ_{SFR}) is the SFR density in ($M_{\odot} \text{ yr}^{-1} \text{ kpc}^{-2}$), Σ_{gas} is the gas surface density ($M_{\odot} \text{ pc}^{-2}$), N is the power-law index, and A is a proportionality constant. In normal SF galaxies, the

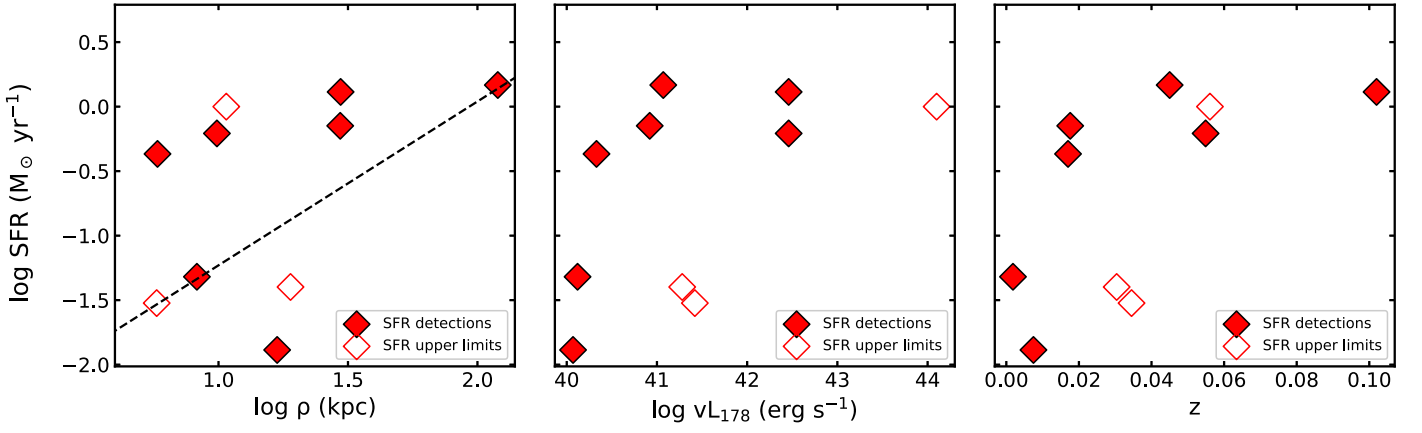


Figure 4. Star formation rates in radio MOHEGs in correlation with nearest-neighbor distances (panel 1), 178 MHz luminosities (panel 2), and redshift (panel 3). The dashed line in panel 1 represents the best line fit obtained from the Theil–Sen slope estimator for the possible correlation. The filled symbols represent cases of detection, and empty symbols denote upper limits.

KS law governs star formation by a power-law scaling with a positive index ($N \sim 1.4$), implying that the disk-averaged SFR per unit area has a linear relation with the total surface gas densities (atomic and molecular gas) on a logarithmic scale (Kennicutt 1998a). We derived the SFRs ($M_{\odot} \text{ yr}^{-1}$) from the $7.7 \mu\text{m}$, as well as the $11.3 \mu\text{m}$ PAH emission lines through the SFR relation given by Ogle et al. (2010), and converted it into Σ_{SFR} ($M_{\odot} \text{ yr}^{-1} \text{ kpc}^{-2}$) assuming a slit width area of $3''.7 \times 10''0$, which was used to extract the IR spectra at $10 \mu\text{m}$. We also used the $70 \mu\text{m}$ line luminosities from PACS & MIPS photometric data (Shi et al. 2005; Meléndez et al. 2014; Lanz et al. 2016) to calculate the SFRs, using the relation derived by Calzetti et al. (2010), and converted it into Σ_{SFR} ($M_{\odot} \text{ yr}^{-1} \text{ kpc}^{-2}$) assuming the circular aperture used for the photometry of radii $12''$ for PACS and $30''$ for MIPS. We used Equation (5),

$$\Sigma_{\text{H}_1+\text{H}_2} (M_{\odot} \text{ pc}^{-2}) = \frac{N_{\text{H}_1} + 2N_{\text{H}_2}}{1.25 \times 10^{20} \text{ cm}^{-2}} \text{ cm}^{-2}, \quad (5)$$

to convert column densities into surface densities. To maintain consistency with Kennicutt (1998a), we parameterized the gas surface densities ($\Sigma_{\text{H}_1+\text{H}_2}$) in terms of HI surface densities.

From Figure 5, we see that SFRs derived from all three tracers are comparable with a slightly better correlation (less scatter) for the SFRs derived from the $7.7 \mu\text{m}$ and the $11.3 \mu\text{m}$ data for our sample. The variation in the slope is also within the error bars, and no significant change in star formation densities is observed. Ogle et al. (2010) suggested that $11.3 \mu\text{m}$ PAH-based SFRs should be used cautiously and considered as upper limits. Therefore, we consider SFRs based on $7.7 \mu\text{m}$ PAH lines to study the KS relation in our sample. In radio MOHEGs, there is a very weak correlation of the total hydrogen gas surface densities ($\Sigma_{\text{H}_1+\text{H}_2}$) with the SFR densities (Σ_{SFR}) calculated from the $7.7 \mu\text{m}$ PAH lines. The correlation coefficient value τ_k is 0.24 with a p -value of 0.32. The association between the SFR densities and the gas surface densities vanishes when we consider only the neutral gas surface densities with $\tau_k = 0.06$, which agrees well with earlier studies of molecular-rich spiral galaxies that the total cold gas (HI + H₂) densities or molecular gas densities influence the SFRs significantly compared to neutral gas (Wong & Blitz 2002). In addition, a tighter correlation is observed

between SFR densities (Σ_{SFR}) and molecular gas surface densities (Σ_{H_2}) in radio MOHEGs with $\tau_k = 0.33$ with a p -value of 0.17.

In Figure 6 we present a comparative analysis of radio MOHEGs alongside ETGs to determine the relation between these galaxy types and the KS law. We do not study SF relations with molecular gas because radio MOHEGs are H₂ dominated, and this would follow the same trend as for total gas densities. SF galaxies like spirals and starburst galaxies from the sample (Kennicutt 1998a) tend to lie on the empirically established KS law with an index of $N = 1.41 \pm 0.07$ of the power-law fit. However, Kennicutt & De Los Reyes (2021) established a better power-law fit for a combined KS law for 119 galaxies, with a slope $N = 1.50 \pm 0.05$, which is steeper than was found by Kennicutt (1998a). ETGs deviate from the combined KS relation, the best-fit line has a slope of 1.14 ± 0.04 for a sample of the ATLAS^{3D} survey of ETGs. The ETGs, compared to spirals and starburst galaxies, have comparably lower average SFR surface densities (Davis et al. 2014). Radio MOHEGs exhibit a wide range of gas surface densities from 33 to 1844 $M_{\odot} \text{ pc}^{-2}$. In terms of the gas surface densities, radio MOHEGs reside between the low and high extremes of gas densities observed in starburst galaxies and normal spirals from Kennicutt’s sample (Kennicutt 1998a), respectively. Our analysis suggests that radio MOHEGs consistently deviate from the combined KS relation, indicating lower star formation surface densities than the central regions of normal SF galaxies and ETGs. This result emphasizes that radio MOHEGs emerge as a unique class of galaxies with an indication of lower star formation densities despite the abundance of molecular gas, as seen in Figure 6. For radio MOHEGs, we report a star formation relation (SFR derived from $7.7 \mu\text{m}$) with total hydrogen surface densities with a power-law index of $N \simeq 1.579 \pm 0.305$ and $A \simeq -5.318 \pm 0.726$ (computed using the Akritas–Theil–Sen non-parametric line estimator using the NADA package in R software) and can be written as

$$\log [\Sigma_{\text{SFR}} (M_{\odot} \text{ yr}^{-1} \text{ kpc}^{-2})] = (1.579 \pm 0.305) \times \log [\Sigma_{\text{H}_1+\text{H}_2} (M_{\odot} \text{ pc}^{-2})] - (5.318 \pm 0.726). \quad (6)$$

We also infer that using different tracers for SFRs does not alter the position of radio MOHEGs in the KS law relation. The molecular gas mass derived from H₂ rotational lines and CO

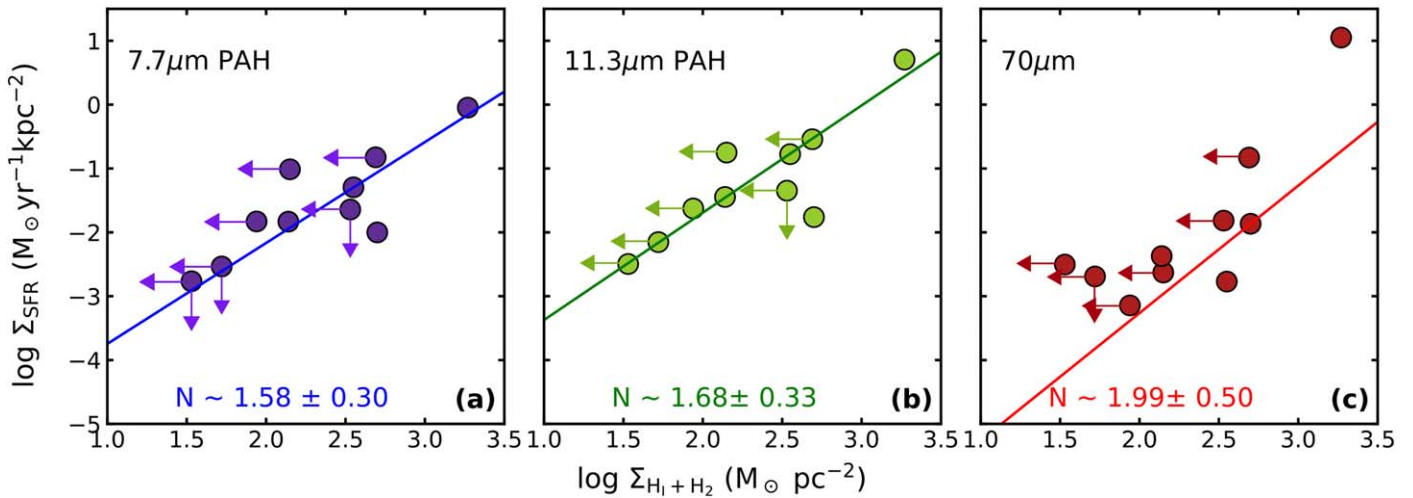


Figure 5. Comparison of the KS relation for radio MOHEGs based on different tracers of SFRs. The SFRs are computed using the luminosity of the (a) $7.7 \mu\text{m}$ PAH luminosities, (b) $11.3 \mu\text{m}$ PAH luminosities, and (c) $70 \mu\text{m}$ luminosities. N is the slope value for the best line fit estimated from the Theil–Sen slope estimator. The arrows represent upper limits on the x - and y -axes.

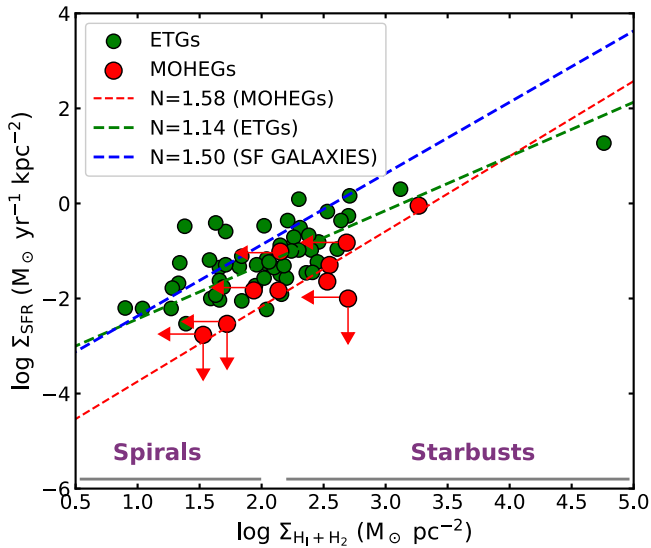


Figure 6. The KS law of star formation with the hydrogen gas (atomic + molecular) surface densities for normal SF and starburst galaxies. The power-law fit for SF galaxies is taken from Kennicutt & De Los Reyes (2021), and that of ETGs from Davis et al. (2014) compared with the star formation relations in radio MOHEGs. The surface density of the gas is determined from C0 (2-1) emission for ETGs and SF galaxies, while for radio MOHEGs, it is determined from H_2 rotational line transitions (Ogle et al. 2010). The red arrows represent upper limits on the x - and y -axes.

observations may have different systematics and may cause some offset in the KS law relation. It will be worth checking with a larger sample in the future whether the offset seen here arises only due to these systematics.

4. HI Absorption Surveys and Prospects with SKA

Galaxies such as radio MOHEGs are expected to have lower HI column densities, which make it difficult to detect them in emission surveys with current radio instruments. HI absorption studies against bright radio continuum background can track the neutral hydrogen in galaxies, which otherwise could not be seen in HI emission observations due to the constraints of the achievable sensitivities at larger distances (Morganti & Osterloo 2018; Dutta et al. 2022). HI surveys offer substantial

advantages to trace the star formation and galaxy evolution from nearby to the distant universe due to their independence of the effects of extinction by dust and color. Hydrogen structures in the inner disk regions, spiral arms, tails, filaments, emission, and absorption profiles tracing the interaction and mergers in galaxies have been regularly detected with the SKA pathfinder instruments such as the ATCA, MeerKAT, uGMRT, VLA, ASKAP, and WSRT (Morganti & Osterloo 2018; Koribalski et al. 2020). HI absorption surveys for MOHEG-type sources will enlarge our sample and help us to better understand the hydrogen gas picture in these galaxies (Wagh et al. 2023).

The sensitivity of HI detections in MOHEG-type galaxies at different flux densities, observation times, and redshifts are plotted in Figures 7 and 8 for SKA1-MID, SKA2, MeerKAT, and uGMRT. The HI absorption limits depend on the strength of the background continuum $F_{1.4 \text{ GHz}}$ flux density, the system equivalent flux density (SEFD) of the radio telescopes, the total on-source integration time, and the FWHM, that is, the half-width of the spectral line. Figure 7 shows $N(\text{HI})$ absorption detection limits based on extrapolated flux densities at a median redshift for different instruments at different integration times. We used the 178 MHz fluxes of the radio MOHEGs (Ogle et al. 2010), and we consider that the MOHEG-type sources would have the same luminosities at five times the luminosity distance as the current sources. We derived the respective 178 MHz fluxes. We then extrapolated these flux densities at a redshifted HI observing line frequency at the median redshift of the total sample using a power-law scaling of -0.7 spectral index (typical value for radio galaxies). Further, taking these flux densities as the background continuum strength values, we calculate 5σ sensitivity limits on HI detections for different instruments at different integration times (see Appendix for more details). The theoretical rms noise was calculated for a given integration time at a 5 km s^{-1} channel width for all the instruments (Blyth et al. 2015; Braun et al. 2019; Maddox et al. 2021). With a strong background continuum and reasonable integration times of up to ~ 10 hr, the SKA1-MID and SKA2 bands will detect sources with $N(\text{HI})$ column densities as low as $\sim 10^{17} \text{ cm}^{-2}$, as compared to MeerKAT and uGMRT. The column density $N(\text{HI})$ absorption detection limits as a function

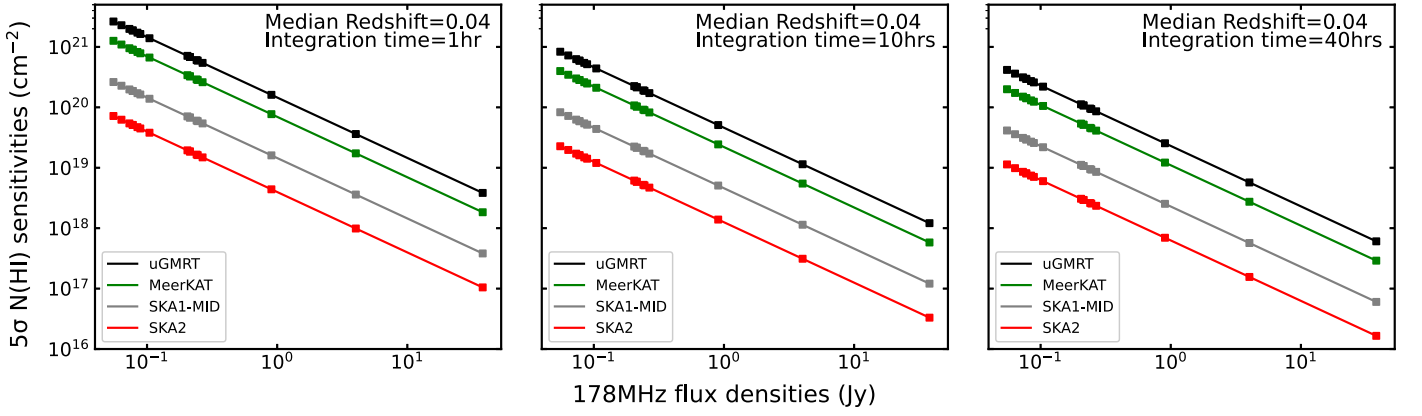


Figure 7. $5\sigma N(\text{H I})$ absorption sensitivities for MOHEG-type sources for SKA1-MID (gray line), SKA2 (red line), and the pathfinder instruments MeerKAT (green line) and uGMRT (black line) for 1 hr (panel 1), 10 hr (panel 2), and 40 hr (panel 3) integration times for a range of flux densities at 178 MHz.

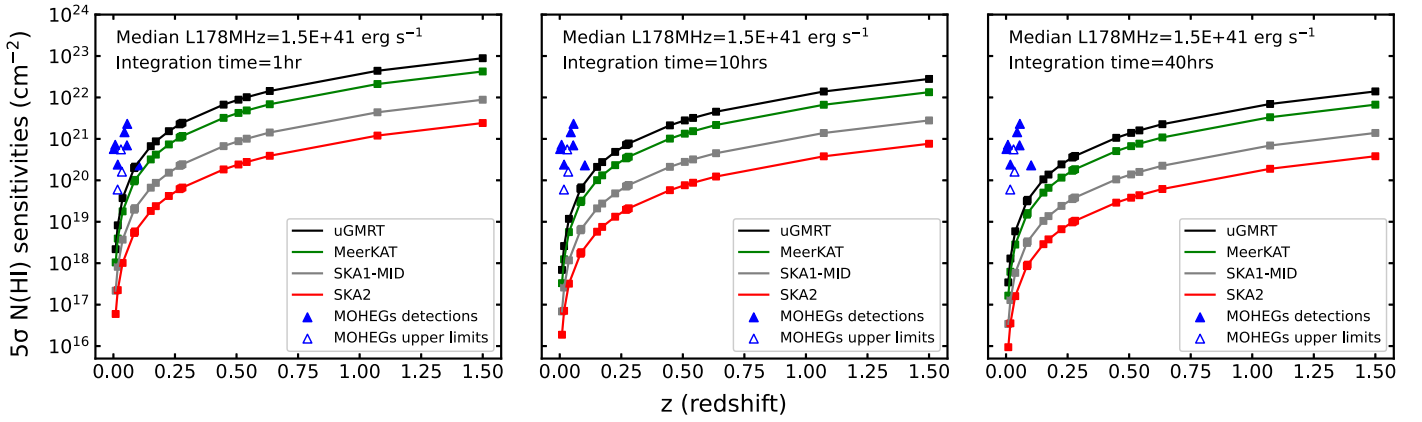


Figure 8. $5\sigma N(\text{H I})$ absorption sensitivities for MOHEG-type sources for SKA1-MID (gray line), SKA2 (red line), and the pathfinder instruments MeerKAT (green line) and uGMRT (black line) for 1 hr (panel 1), 10 hr (panel 2), and 40 hr (panel 3) integration times for a range of redshifts. The radio MOHEG sample is plotted as blue triangles.

of redshift and integration times are shown in Figure 8 along with the radio MOHEG sample plotted as blue triangles. To generate these plots, the median luminosity at 178 MHz was extrapolated to the corresponding redshifted HI line frequencies. These plots suggest that in shallow surveys with a reasonable integration time of ~ 1 hr, SKA1-MID and SKA2 will efficiently detect $N(\text{H I})$ column densities as low as $\sim 10^{21} \text{ cm}^{-2}$ up to redshift of $z \sim 1.5$ for a bright population of background sources, thereby probing the cosmic noon regime in which the star formation activities show a peak. On the other hand, focused (~ 10) and deep (~ 40 hr) pointed observations will detect column densities as low as $\sim 10^{20} \text{ cm}^{-2}$ at $z \sim 1.5$ and $\sim 10^{17} \text{ cm}^{-2}$ column densities in the $z \sim 0$ range. Thus, a new class of low column density features can be detected in galaxies with different morphologies that reside in diverse environments. This will provide unprecedented information on the gas interaction in galaxies, their evolution, and the impact of the surrounding environment on their capacity for star formation. The SKA will efficiently detect low column density features tracing the complete gas cycle from disks to the IGM along with tails and filaments, indicating the phase (pre, post, or ongoing) of merger events and AGN-induced feedback mechanisms. More importantly, it will also provide the complete data for tracing the full picture of the HI universe from the current epoch up to cosmic noon in a reasonable

observation time and will allow us to probe the star formation history of the universe.

5. Summary and Conclusion

In this work, we presented a study of hydrogen gas in a sample of radio MOHEGs, focusing on studying the distribution and kinematics of HI and its influence on star formation relations using the HI 21 cm absorption line in this sample and prospects with the SKA and pathfinders for conducting these studies. The main results of this work are summarized below.

1. The radio MOHEGs exhibit a deficiency in atomic hydrogen with a median value lower than or equal to $5.65 \times 10^{20} \text{ cm}^{-2}$ as compared to merging galaxies at similar redshifts. However, this can be an order of magnitude higher if the atomic gas predominantly coexists at the same temperature with the unusually warmer molecular gas.
2. The molecular fraction in the radio MOHEGs is dominated by the H_2 gas, with a median $f_{\text{H}_2} \leq 0.96$.
3. There exists no clear correlation between HI gas or total hydrogen ($\text{HI} + \text{H}_2$) gas column densities and the physical properties of the galaxy such as nearest-neighbor distances and radio jet luminosities. The total hydrogen gas densities in the radio MOHEGs provide a complete estimate of gas reservoirs available for star formation, and

a possible weak correlation with the SFRs is anticipated in our sample.

4. For our sample, SFRs show a possible but weak positive correlation with nearest-neighbor distances, implying that interactions can influence the star formation activities.
5. Radio MOHEGs show indications of lower surface densities of star formation compared to SF galaxies and ETGs. They also show an indication of an offset from the power-law trends established for SF galaxies and ETGs.
6. We can detect lower HI column densities (10^{17} cm^{-2}) through HI absorption surveys of the SKA1-MID and SKA2 bands. This will generate statistical data to improve the constraints on the evolution of SFRs on cosmic timescales and probe the star formation history of the Universe from the current epoch up to $z \sim 2$ and beyond for MOHEG-type sources.

Radio MOHEGs belong to cluster environments or interacting groups/pairs; feedback from neighboring galaxy collisions and tidal interactions may impact the ISM. This might be the reason for the excess H_2 gas. Feedback from these interactions can also heat the H_2 gas. The density of the environments in which these galaxies reside also plays an important role in their interaction with the ISM. Quantifying the interaction effects and their impact on the H_2 excitation will give us more insights into the feedback through galaxy interactions in these galaxies. Radio jet luminosities are not a good measure of energy transferred into the ISM via jets because there is significant Doppler enhancement in relativistic jets. The study of the isotropic properties of the material thrown out from the jets to radio lobes gives us a better estimate of the kinetic luminosities of the jet. Deep X-ray observations and radio observations of the lobe structures can emphasize better estimates of the plasma states and, hence, of the jet kinetic luminosities (Punsly 2005). Calculating kinetic luminosities of the radio MOHEGs will be consequential in quantifying the impact of AGN-jet feedback on the molecular and atomic gas phases. The cold H_2 ($< 100 \text{ K}$) gas distribution is not systematically studied for radio MOHEGs sample; the molecular fraction derived from CO observations will help us to better understand the role of cold

H_2 in the star formation processes. Understanding the neutral and molecular hydrogen gas is crucial for understanding the galaxy evolution and their star formation activities. Reinforcing the weak correlations with a larger sample for radio MOHEGs would help us understand the kinematics of these sources better. Radio MOHEGs are interesting objects for examining the interplay between SFRs and feedback processes within radio galaxies.

Acknowledgments

We thank the anonymous referee for providing valuable comments that enhanced the quality of this paper. S.W., N.R., M.P., A.M., C.M., and B.G. gratefully acknowledge the support of the Indo-French Centre for the Promotion of Advanced Research (Centre Franco-Indien pour la Promotion de la Recherche Avancée) under project 6504-3.

Appendix Details of HI Sensitivity Calculations

Using the following equation, we calculate the $N(\text{HI})$ absorption sensitivities of each instrument using the following equation:

$$N_{\text{HI}} = 1.82 \times 10^{18} \cdot \frac{T_s}{f_c} \cdot \frac{5(\text{RMS})}{S_{1.4}} \cdot \sqrt{2\pi} \sigma_l \cdot \sqrt{\frac{\Delta v_{\text{ch}}}{\sigma_l}} \text{ cm}^{-2}. \quad (\text{A1})$$

T_s is the spin temperature of HI gas, assumed to be 100 K (Dutta 2019). f_c is the fraction of the background radio source covered by the absorbing gas, taken as 1. rms is the noise per 5 km s^{-1} channel. $S_{1.4}$ is the flux density value at 1.4 GHz $\sigma_l = \text{FWHM}/2.35$, this is the HI line width; the FWHM is assumed to be 100 km s^{-1} because the maximum FWHM for MOHEGs sources is around 100 km s^{-1} .

The extra factor of $\sqrt{\frac{\Delta v_{\text{ch}}}{\sigma_l}}$ comes into the picture as we are calculating the sensitivities after smoothing the spectra to the spectral resolution of the HI line widths. Δv_{ch} is the channel width, i.e., 5 km s^{-1} . Refer to Table 4.






Table 4
HI Absorption Sensitivities for Different Telescopes

Instrument	rms mJy/beam/ 5 km s^{-1}	Total Integration Time hr	$N_{\text{HI}(5\sigma)}$ cm^{-2}	Reference for rms
uGMRT	1.044	1	8.77E+22	^a
MeerKAT	0.500	1	4.20E+22	(Maddox et al. 2021)
SKA1-MID	0.104	1	8.75E+21	(Braun et al. 2019)
SKA2	0.009	1	2.43E+21	(Blyth et al. 2015)

Note. 5σ sensitivities calculated using a minimum background flux density of $0.39 \text{ mJy beam}^{-1}$.

^a <http://www.ncra.tifr.res.in:8081/~secr-ops/etc/rms/rms.html>

ORCID iDs

Sai Wagh  <https://orcid.org/0009-0006-5549-5196>
 Mamta Pandey-Pommier  <https://orcid.org/0000-0001-5829-1099>
 Nirupam Roy  <https://orcid.org/0000-0001-9829-7727>
 Md Rashid  <https://orcid.org/0009-0007-0120-5728>
 Alexandre Marcowith  <https://orcid.org/0000-0002-3971-0910>

References

- Alladin, S. M. 1975, *BASI*, **3**, 5
 Allison, J. R., Sadler, E. M., & Meekin, A. M. 2014, *MNRAS*, **440**, 696
 Antonuccio-Delogu, V., & Silk, J. 2008, *MNRAS*, **389**, 1750
 Baars, J. M., Genzel, R., et al. 1977, *AA*, **61**, 99
 Bergeron, J., & Boissé, P. 1991, *A&A*, **243**, 344
 Blitz, L., & Rosolowsky, E. 2004, *ApJL*, **612**, L29
 Blitz, L., & Rosolowsky, E. 2006, *ApJ*, **650**, 933
 Blyth, S., van der Hulst, T. M., Verheijen, M. A. W., et al. 2015, *Proc. of Advancing Astrophysics with the Square Kilometre Array (AASKA14)*, 128
 Boselli, A., Fossati, M., & Sun, M. 2022, *A&ARv*, **30**, 3
 Braun, R., Bonaldi, A., Bourke, T., Keane, E., & Wagg, J. 2019, arXiv:1912.12699
 Brown, T., Catinella, B., Cortese, L., et al. 2017, *MNRAS*, **466**, 1275
 Calzetti, D., Wu, S. Y., Hong, S., et al. 2010, *ApJ*, **714**, 1256
 Chandola, Y., Gupta, N., & Saikia, D. J. 2013, *MNRAS*, **429**, 2380
 Chung, A., van Gorkom, J. H., Kenney, J. D. P., Crowl, H., & Vollmer, B. 2009, *AJ*, **138**, 1741
 Cielo, S., Babul, A., Antonuccio-Delogu, V., Silk, J., & Volonteri, M. 2018, *AA*, **617**, A58
 Clark, B. G. 1965, *ApJ*, **142**, 1398
 Cluver, M. E., Appleton, P. N., Ogle, P., et al. 2013, *ApJ*, **765**, 93
 Colgan, S. W. J., Salpeter, E. E., & Terzian, Y. 1990, *ApJ*, **351**, 503
 Cox, D. P., & Smith, B. W. 1974, *ApJL*, **189**, L105
 Curran, S. J., Duchesne, S. W., Divoli, A., & Allison, J. R. 2016, *MNRAS*, **462**, 4197
 Davis, T. A., Young, L. M., Crocker, A. F., et al. 2014, *MNRAS*, **444**, 3427
 Dénes, H., Kilborn, V. A., Koribalski, B. S., & Wong, O. I. 2016, *MNRAS*, **455**, 1294
 Dutta, R. 2019, *JApA*, **40**, 41
 Dutta, R., Kurapati, S., Aditya, J. N. H. S., et al. 2022, *JApA*, **43**, 103
 Dutta, R., Srikanand, R., & Gupta, N. 2019, *MNRAS*, **489**, 1099
 Dwarakanath, K. S., Owen, F. N., & van Gorkom, J. H. 1995, *ApJL*, **442**, L1
 Emonts, B. H. C., Morganti, R., Struve, C., et al. 2010, *MNRAS*, **406**, 987
 Fabian, A. C. 1994, *ARAA*, **32**, 277
 Fanaroff, B. L., & Riley, J. M. 1974, *MNRAS*, **167**, 31P
 Federman, S. R., Glassgold, A. E., & Kwan, J. 1979, *ApJ*, **227**, 466
 Foley, N., Cazaux, S., Egorov, D., et al. 2018, *MNRAS*, **479**, 649
 Fujita, Y., Kawakatu, N., & Nagai, H. 2022, *ApJ*, **924**, 24
 Gentile, G., Rodríguez, C., Taylor, G. B., et al. 2007, *ApJ*, **659**, 225
 Geréb, K., Maccagni, F. M., Morganti, R., & Oosterloo, T. A. 2015, *A&A*, **575**, A44
 Guglielmo, V., Poggianti, B. M., Moretti, A., et al. 2015, *MNRAS*, **450**, 2749
 Guillard, P., Ogle, P. M., Emonts, B. H. C., et al. 2012, *ApJ*, **747**, 95
 Hollenbach, D. J., Werner, M. W., & Salpeter, E. E. 1971, *ApJ*, **163**, 165
 Jaffe, W., & McNamara, B. R. 1994, *ApJ*, **434**, 110
 Kanekar, N., Braun, R., & Roy, N. 2011, *ApJL*, **737**, L33
 Kawata, D., & Mulchaey, J. S. 2008, *ApJL*, **672**, L103
 Kennicutt, R. C. J. 1998a, *ApJ*, **498**, 541
 Kennicutt, R. C. J. 1998b, *ARAA&A*, **36**, 189
 Kennicutt, R. C. J., & De Los Reyes, M. A. C. 2021, *ApJ*, **908**, 61
 Knapp, G. R., Kerr, F. J., & Williams, B. A. 1978, *ApJ*, **222**, 800
 Koribalski, B. S., Staveley-Smith, L., Westmeier, T., et al. 2020, *Ap&SS*, **365**, 118
 Lada, C. J. 2005, *PThPS*, **158**, 1
 Lanz, L., Ogle, P. M., Alatalo, K., & Appleton, P. N. 2016, *ApJ*, **826**, 29
 Le Bourlot, J., Pineau des Forêts, G., & Flower, D. R. 1999, *MNRAS*, **305**, 802
 Leroy, A. K., Walter, F., Brinks, E., et al. 2008, *AJ*, **136**, 2782
 Li, M., Ostriker, J. P., Cen, R., Bryan, G. L., & Naab, T. 2015, *ApJ*, **814**, 4
 Maddox, N., Frank, B. S., Ponomareva, A. A., et al. 2021, *A&A*, **646**, A35
 Mahony, E. K., Morganti, R., Emonts, B. H. C., Oosterloo, T. A., & Tadhunter, C. 2013, *MNRAS*, **435**, L58
 Mahony, E. K., Oonk, J. B. R., Morganti, R., et al. 2016, *MNRAS*, **455**, 2453
 Maiolino, R. 2017, *Natur*, **544**, 202
 Man, A. M., & Sirio, B. 2018, *NatAs*, **2**, 695
 Maret, S., Bergin, E. A., Neufeld, D. A., et al. 2009, *ApJ*, **698**, 1244
 Martizzi, D., Faucher-Giguère, C.-A., & Quataert, E. 2015, *MNRAS*, **450**, 504
 Meléndez, M., Mushotzky, R. F., Shimizu, T. T., Barger, A. J., & Cowie, L. L. 2014, *ApJ*, **794**, 152
 Morganti, R., Murthy, S., Oosterloo, T., et al. 2023, *A&A*, **678**, A42
 Morganti, R., & Oosterloo, T. 2018, *A&ARv*, **26**, 1
 Morganti, R., Oosterloo, T. A., Emonts, B. H. C., van der Hulst, J. M., & Tadhunter, C. N. 2003, *ApJL*, **593**, L69
 Morganti, R., Tadhunter, C. N., & Oosterloo, T. A. 2005, *A&A*, **444**, L9
 Moss, V. A., Allison, J. R., Sadler, E. M., et al. 2017, *MNRAS*, **471**, 2952
 Naab, T., & Ostriker, J. P. 2017, *ARAA&A*, **55**, 59
 Narayanan, D., Cox, T. J., Kelly, B., et al. 2008, *ApJS*, **176**, 331
 Nesvadba, N. P. H., Boulanger, F., Salomé, P., et al. 2010, *A&A*, **521**, A65
 Noordermeer, E., van der Hulst, J. M., Sancisi, R., Swaters, R. A., & van Albada, T. S. 2005, *A&A*, **442**, 137
 Ogle, P., Antonucci, R., Appleton, P. N., & Whysong, D. 2007, *ApJ*, **668**, 699
 Ogle, P., Boulanger, F., Guillard, P., et al. 2010, *ApJ*, **724**, 1193
 Pan, H.-A., Lin, L., Hsieh, B.-C., et al. 2018, *ApJ*, **868**, 132
 Park, G., Lee, M.-Y., Bialy, S., et al. 2023, *ApJ*, **955**, 2
 Pearson, W. J., Wang, L., Alpaslan, M., et al. 2019, *A&A*, **631**, A51
 Peng, Y., Maiolino, R., & Cochrane, R. 2015, *Natur*, **521**, 192
 Punsly, B. 2005, *ApJL*, **623**, L9
 Rauch, M. 1998, *ARAA&A*, **36**, 267
 Rohlfs, K., & Wilson, T. L. 2000, *Tools of Radio Astronomy* (New York: Springer)
 Rupke, D. S. N., & Veilleux, S. 2011, *ApJL*, **729**, L27
 Saury, E., Miville-Deschênes, M. A., Hennebelle, P., Audit, E., & Schmidt, W. 2014, *A&A*, **567**, A16
 Schmidt, M. 1959, *ApJ*, **129**, 243
 Schmidt, M. 1963, *ApJ*, **137**, 758
 Schulz, R., Morganti, R., Nyland, K., et al. 2021, *A&A*, **647**, A63
 Serra, P., Oosterloo, T., Morganti, R., et al. 2012, *MNRAS*, **422**, 1835
 Shi, Y., Rieke, G. H., Hines, D. C., et al. 2005, *ApJ*, **629**, 88
 Silk, J. 2013, *ApJ*, **772**, 112
 Stecher, T. P., & Williams, D. A. 1967, *ApJL*, **149**, L29
 Struve, C., & Conway, J. E. 2010, *A&A*, **513**, A10
 Thi, W. F., Hocuk, S., Kamp, I., et al. 2020, *A&A*, **634**, A42
 Toomre, A. 1974, in *Proc. from IAU Symp. 58, The Formation and Dynamics of Galaxies*, ed. J. R. Shakeshaft, 347
 van Gorkom, J. H., Knapp, G. R., Ekers, R. D., et al. 1989, *AJ*, **97**, 708
 Veilleux, S., Bolatto, A., Tombesi, F., et al. 2017, *ApJ*, **843**, 18
 Vidali, G. 2013, *ChRv*, **113**, 8752
 Vollmer, B. 2013, in *Planets, Stars and Stellar Systems*, Vol. 6, ed. T. D. Oswalt & W. C. Keel (Berlin: Springer), 207
 Wagh, S., Pandey-Pommier, M., Roy, N., et al. 2023, in *Proc. of the Annual Meeting of the French Society of Astronomy and Astrophysics (SF2A-2023)*, ed. M. N'Diaye et al., 71
 Wang, J., Koribalski, B. S., Serra, P., et al. 2016, *MNRAS*, **460**, 2143
 Weżgowiec, M., Bomans, D. J., Ehle, M., et al. 2012, *A&A*, **544**, A99
 Winkel, B., Wiesemeyer, H., Menten, K. M., et al. 2017, *A&A*, **600**, A2
 Wolfe, A. M., Gawiser, E., & Prochaska, J. X. 2005, *ARAA&A*, **43**, 861
 Wolfire, M. G., Hollenbach, D., McKee, C. F., Tielens, A. G. G. M., & Bakes, E. L. O. 1995, *ApJ*, **443**, 152
 Wolfire, M. G., McKee, C. F., Hollenbach, D., & Tielens, A. G. G. M. 2003, *ApJ*, **587**, 278
 Wong, T., & Blitz, L. 2002, *ApJ*, **569**, 157
 Wright, E. L. 2006, *PASP*, **118**, 1711
 Yun, M. S., Ho, P. T. P., & Lo, K. Y. 1994, *Natur*, **372**, 530